

Mapping global offshore wind resource: wake losses, optimisation potential and climate effects

Simon C. Warder^a, Matthew D. Piggott^a

^a*Department of Earth Science and Engineering, Imperial College London, London, SW7 2BP, UK*

Abstract

In this work, we assess global offshore wind energy resources, wake-induced losses, array layout optimisation potential and climate change impacts. We first map global offshore ambient wind resource from reanalysis data. We estimate wake-induced losses using an engineering wake model, revealing that locations with low (high) resource typically experience larger (smaller) percentage losses. However, we further find that the specific wind speed distribution is important, with narrower distributions generally leading to greater losses. This is due to the overlap between the wind speed distribution and the high-sensitivity region of the turbine thrust and power curves. Broadly, this leads to much stronger wake-induced losses in the tropics (which experience the trade winds) than mid-latitudes. However, the tropics also experience a narrower wind direction distribution; our results demonstrate that this leads to greater potential for mitigation of wake effects via layout optimisation. Finally, we assess projected changes in wind resource and wake losses due to climate change under a high-emission scenario. Many regions are projected to decrease in ambient wind resources, and furthermore these regions will typically experience greater wake-induced losses, exacerbating the climate impact. These results highlight the different challenges and opportunities associated with exploiting offshore wind resources across the globe.

Keywords: Offshore wind, wake losses, array layout optimisation, climate change

1. Introduction

Renewable energy is rapidly expanding across the world (Hassan et al., 2024). Offshore wind in particular is undergoing a phase of unprecedented growth and falling costs (Li et al., 2022). As of December 2023 there was a total of 75.2 GW of offshore wind installed capacity, with a further 138 GW expected to be added by 2028 (GWEC, 2024), including within a number of emerging markets.

To date, 45% of global offshore wind has been installed in Europe (GWEC, 2024), and a large number of studies have investigated current (deCastro et al., 2019; Hasager et al., 2020; Martinez and Iglesias, 2022b) and future (deCastro et al., 2019; Martinez and Iglesias, 2021; Hahmann et al., 2022; Martinez et al., 2023) wind resources in this region, as well as implications for energy/power system modelling (Fernández-Guillamón et al., 2019; Lyden et al., 2024; Glaum et al., 2024). Due to the imminent global expansion of offshore wind, there are a growing number of studies considering current and/or future wind resource in other regions such as the USA (e.g. Costoya et al., 2020), South America (e.g. Pimenta et al., 2019; Vinhoza and Schaeffer, 2021; Shadman et al., 2023), Asia (e.g. Dinh et al., 2022; Patel et al., 2022; Abdullah et al., 2023) or globally (e.g. Bandoc et al., 2018; Weiss et al., 2018; Soares et al., 2020).

A number of popular tools exist that are dedicated to mapping wind resources. These include so-called ‘wind atlas’ products, such as the New European Wind Atlas (Hahmann et al., 2020; Dörenkämper et al., 2020) and Global Wind Atlas (Davis et al., 2023). Both are based on ERA-5

hindcast data (Hersbach et al., 2020), dynamically downscaled using the Weather Research and Forecasting (WRF) model (Powers et al., 2017), with ‘microscale’ modelling via the WAsP software suite (Mortensen et al., 2001). Reanalysis products are also used directly for wind resource mapping (e.g. Soares et al., 2020; Gruber et al., 2022). Either reanalyses or wind atlases are commonly used as inputs into energy systems models (ESMs), which are in turn used to inform policy decisions regarding future energy mix and infrastructure. One popular tool providing ESM wind power inputs is the Renewables.Ninja project (Staffell and Pfenninger, 2016), which is based on bias-corrected reanalysis data. In the climate context, wind resource mapping is commonly undertaken using either global projection model outputs such as from CMIP5 (e.g. Reyers et al., 2016; Zheng et al., 2019) or CMIP6 (e.g. Ibarra-Berastegui et al., 2023), or using downscaled climate products such as from the CORDEX project (e.g. Li et al., 2020; Molina et al., 2022; Akperov et al., 2023), or other downscaling methods (e.g. Zhang and Li, 2021; Fernández-Alvarez et al., 2023).

An important aspect to assessing potential wind resource extraction is power loss due to turbine wake effects (Jensen, 1983). The extraction of kinetic energy by a wind turbine reduces the wind speed immediately downstream, impacting the power output from any downstream turbines within the same farm (so-called ‘intra-farm’ or ‘internal’ wakes). This effect also arises at larger spatial scales, where an upstream wind farm can reduce the power output of a downstream farm (Lundquist et al., 2019; Schneemann et al., 2020; Cañadillas et al., 2022), resulting in so-called ‘inter-farm’ or ‘cluster’ wakes. In the intra-farm case, average wake effects will depend on the turbine type and the layout of the wind farm, and in the inter-farm case on the size, density, capacity and relative positions of the farms. However, in both cases, another important factor is the local distribution of wind speed and direction. The wind speed is important since wake effects can only impact power output while the wind speed is greater than the turbine’s cut-in speed, but not significantly greater than the rated speed. The wind direction is important because a given pair of turbines or farms only interact when the wind direction is (broadly) aligned with their relative positions.

Intra-farm wake effects are well studied in the context of optimal layout design (Elkinton et al., 2008; Samorani, 2013; Shakoor et al., 2016; Piggott et al., 2022) and optimal wind farm control (Menezes et al., 2018; Kheirabadi and Nagamune, 2019). A number of modelling and optimisation approaches have emerged for the intra-farm wake problem (Göçmen et al., 2016), including via CFD simulations (Sanderse et al., 2011), so-called ‘engineering’ wake models (Archer et al., 2018), or more recently using machine learning surrogate models trained using either CFD model-generated training data (e.g. Ti et al., 2020; Zhang and Zhao, 2020; Purohit et al., 2022; Li et al., 2023), or directly from observation data (e.g. Ashwin Renganathan et al., 2022).

However, despite the breadth of literature on wake effects, their incorporation into resource assessment tools or studies is limited. In the climate context, Hahmann et al. (2022) use an engineering wake model to include wake-induced losses of a proposed wind farm cluster, within a study of the climate impact on wind energy resources in the North Sea. Wärder and Piggott (2024) study the evolution of wake effects (on various spatial scales) with climate change, based on a near-future set of wind farms in the German Bight, finding statistically significant changes in wake effects during the summer months. In the reanalysis context, and in particular for models used as inputs into ESMs, wake effects may be implicitly accounted for via bias correction methods based on matching models to observed capacity factors (Staffell and Pfenninger, 2016; Benmoufok et al., 2024). However, in this case, variation in wake effects either spatially or due to differing wind farm designs would be neglected. Alternatively, wake effects are sometimes explicitly accounted for, e.g. via a fixed ‘array efficiency’ factor (Bosch et al., 2018, 2019), or using pre-computed losses for idealised farms of various sizes (Glaum et al., 2024), such as those found in Volker et al. (2017); Energiewende et al. (2020); Gea-Bermúdez et al. (2022). In reality, however, wake effects vary depending on the specific wind climate experienced at a given location, as well as with climate change (Devis et al.,

2018). Furthermore, the potential to mitigate these losses via array layout optimisation will vary with the wind direction distribution, with narrower distributions likely to offer greater optimisation potential. These factors will have implications for the transfer of knowledge and experience from regions such as Europe, where the offshore wind industry is relatively mature, to emerging markets elsewhere in the world, where the challenges and opportunities associated with wake effects may differ significantly.

With a focus on global spatial variation, the objectives of the present study are to investigate

- (i) the ambient offshore wind resource;
- (ii) the power losses due to intra-farm wake effects for a given wind farm;
- (iii) the layout optimisation potential, which we define as the percentage improvement in wind farm power which can be achieved via layout optimisation, compared with a simple grid layout;
- (iv) the impact of climate change on both ambient offshore wind resource, and intra-farm wake effects.

The remainder of the paper is structured as follows. Section 2 presents the data and methods used within this study, including reanalysis data, climate projection data, and wake modelling and layout optimisation approaches. Corresponding results are presented and discussed in section 3. Finally, we draw conclusions in section 4.

2. Methods

2.1. Data and pre-processing

2.1.1. ERA-5

We utilise reanalysis data from ERA-5 (Hersbach et al., 2020), for the historical period 1995–2014. We use the 100 m u and v wind components, from which we derive the wind speed and direction. The data has a spatial resolution of 0.25° , and hourly temporal resolution. We download data from the Copernicus Climate Data Store at a 6-hourly resolution. From this, we derive the wind rose for each grid cell, based on wind speed bins from 0 to 25 m s^{-1} in steps of 0.5 m s^{-1} , and directional bins of 10° . The use of a wind rose to represent the wind distribution at each location reduces the total volume of data required to represent global wind climate at high resolution.

2.1.2. CMIP6

The future climate scenario we assess in this work is the SSP585 scenario, from which we use the period 2081–2100, using CMIP6 projections. This high-emissions scenario corresponds to intensified fossil fuel exploitation, leading to radiative forcing of 8.5 W m^{-2} by the year 2100, and lies at the upper end of the scenarios considered in the literature. We choose this scenario on the basis that it will produce responses of the greatest magnitude, making it easiest to identify robust trends. We compare this future scenario against corresponding CMIP6 data from the ‘historical’ scenario, using the period 1995–2014.

The specific CMIP6 model outputs we select for this study are based on the availability of both the ‘historical’ and SSP585 scenarios, a nominal resolution of 100 km or finer, and surface wind speeds with daily frequency. Data was searched and downloaded via the Earth System Grid Federation (ESGF) search tool (<https://esgf-ui.ceda.ac.uk/cog/search/cmip6-ceda/>). The resulting 10 models are detailed in table 1.

Each of these models provides the ‘surface’ wind speed, at a nominal height of 10 m. Since we are interested in wind speeds at hub heights, we extrapolate these data to 100 m. For this, we use a power law with an exponent of 0.06, following Carvalho et al. (2021), who chose this value based on typical vertical profiles from ERA-5 data, which is available at both 10 and 100 m. The resulting

Model name	Institute	Resolution	Citation
CESM2-WACCM	National Center for Atmospheric Research (NCAR) – USA	$1.25^\circ \text{ lon} \times 0.938^\circ \text{ lat}$	Danabasoglu et al. (2020)
CMCC-CM2-SR5	Euro-Mediterranean Center on Climate Change (CMCC) Foundation – Italy	$1.25^\circ \text{ lon} \times 0.938^\circ \text{ lat}$	Cherchi et al. (2019)
CMCC-ESM2	Euro-Mediterranean Center on Climate Change (CMCC) Foundation – Italy	$1.25^\circ \text{ lon} \times 0.938^\circ \text{ lat}$	Lovato et al. (2022)
MPI-ESM1-2-HR	Max Planck Institute for Meteorology (MPI-M) – Germany	$0.938^\circ \text{ lat} \times 0.938^\circ \text{ lon}$	Müller et al. (2018)
MRI-ESM2-0	Meteorological Research Institute (MRI) – Japan	$1.125^\circ \text{ lat} \times 1.125^\circ \text{ lon}$	Kawai et al. (2019)
GFDL-CM4	Geophysical Fluid Dynamics Laboratory (NOAA-GFDL) – USA	$1^\circ \text{ lat} \times 1.25^\circ \text{ lon}$	Held et al. (2019)
GFDL-ESM4	Geophysical Fluid Dynamics Laboratory (NOAA-GFDL) – USA	$1^\circ \text{ lat} \times 1.25^\circ \text{ lon}$	Dunne et al. (2020)
INM-CM4-8	Institute for Numerical Mathematics (INM) – Russia	$1.5^\circ \text{ lat} \times 2^\circ \text{ lon}$	Volodin et al. (2019)
INM-CM5-0	Institute for Numerical Mathematics (INM) – Russia	$1.5^\circ \text{ lat} \times 2^\circ \text{ lon}$	Volodin et al. (2017)
TaiESM1	Research Center for Environmental Changes (RCEC) – Taiwan	$1.25^\circ \text{ lat} \times 0.938^\circ \text{ lon}$	Lee and Liang (2020)

Table 1: Summary of CMIP6 models used within this study.

data is converted to a wind rose map (consistent with our treatment of the ERA-5 data described above), then regridded by bilinear interpolation to match the ERA-5 grid.

We further bias-correct the climate projection data against the ERA-5 data. [Warder and Piggott \(2024\)](#) compared several common methods for bias correction, with a quantile mapping method based on fitted Weibull distributions found to perform best. However, since wind speeds are not necessarily well described by Weibull distributions at all locations globally, in this study we employ an empirical quantile mapping method, which was also found by [Warder and Piggott \(2024\)](#) to perform well. The bias correction is derived based on the climate dataset over the period that coincides with the historical ERA-5 data, using the latter as ‘ground truth’. Denoting the empirical cumulative density function (CDF) of the ERA-5 data at a particular grid cell and for a particular wind direction as $F_{\text{ERA-5}}$, and the corresponding CDF from the ‘historical’ climate dataset as F_{hist} , the corrected wind speed w_{corr} is given as a function of the raw wind speed w_{raw} as

$$w_{\text{corr}} = F_{\text{ERA-5}}^{-1}(F_{\text{hist}}(w_{\text{raw}})). \quad (1)$$

Since our approach is based on wind roses, the projected climate data is represented as a discrete probability density function (PDF) at a particular set of speeds. Denoting the raw PDF as $f_{\text{raw}}(w)$ and the corrected PDF as $f_{\text{corr}}(w)$, we assume that

$$f_{\text{corr}}(w_{\text{corr}}) = f_{\text{raw}}(w_{\text{raw}}). \quad (2)$$

The raw PDF therefore directly provides the corrected PDF, but evaluated at the ‘corrected’ speeds given by equation (1). To evaluate the corrected PDF on the original set of wind speeds, we linearly interpolate within the values obtained by equation (2).

2.1.3. Other data

We use global data for marine exclusive economic zones (EEZs) from [Flanders Marine Institute \(2020\)](#), in order to restrict our analysis to plausible offshore regions, and to aggregate results for different countries. However, we leave the inclusion of other practical constraints to wind farm deployment, such as bathymetry, shipping lanes etc, to future work. This study uses a resolution of 0.25° , which would not be sufficient to adequately resolve all such features.

2.2. Mapping wake effects

This study seeks to investigate the influence of wind speed distribution on the magnitude of intra-farm wake effects. Our approach is based on computing wind roses at each grid cell whose centroid is within the EEZs. For each such grid cell, we compute two quantities:

- (i) the ‘ambient’ capacity factor which would be produced by a single turbine within that cell, or equivalently the capacity factor of a wind farm, neglecting all wake effects;
- (ii) the ‘waked’ capacity factor which would be produced by a ‘standard’ wind farm within that cell, accounting for wake effects.

The reference wind turbine we use within this work is the 10 MW reference turbine from IEA Task 37 ([Bortolotti et al., 2019](#)), for which power and thrust curve data is available. Neglecting conversion efficiency, the rated (mechanical) power of this turbine is 10.6 MW. The turbine has a hub height of 119 m and a rotor diameter of 198 m. As our ‘standard’ farm, we take a 10 by 10 square array of such wind turbines, with a spacing of 5 rotor diameters. This farm has a total installed capacity of 1.06 GW. The choice of wind turbine model, turbine separation and total capacity were selected in order to be broadly representative of current and near-future offshore wind farms.

The wind rose at a given grid cell is a discrete probability density function, represented by a two-dimensional array which we denote $f_{s,d}$, where s and d denote a particular wind speed and direction, respectively. The first quantity above, the ambient capacity factor, does not depend on the wind direction. We therefore introduce the marginal wind speed distribution, given by

$$f_s = \sum_d f_{s,d}. \quad (3)$$

The ‘ambient’ capacity factor at a given location can then be estimated directly from the power curve $P(s)$, as

$$\text{CF}_{\text{ambient}} = 100\% \cdot \frac{1}{P_{\max}} \sum_s f_s P(s_{\text{hh}}), \quad (4)$$

where P_{\max} is the nominal or rated power of the turbine, in this case 10.6 MW, and s_{hh} is the wind speed extrapolated to the turbine hub height, which is again performed assuming a power law profile with an exponent of 0.06.

For the second quantity above, the waked capacity factor, our initial focus is on the effect of the wind speed distribution. We therefore again take the marginal wind speed distribution, and for each wind speed, we estimate the power produced by the farm, averaged over all possible rotations of the farm. This is equivalent to assuming that all wind directions are equally likely at a given location. This also has the effect of reducing the sensitivity of the waked power with respect to the specific turbine array layout we have chosen, and the local prevailing wind. I.e., here we wish to exclude variations in wake-induced losses which arise from the alignment (or otherwise) of the principal directions of the farm’s grid layout with the prevailing wind.

To estimate the power output of the wind farm, at a particular 100 m wind speed s and subject to a given rotation (or equivalently a given wind direction) d , we use the engineering wake model of [Bastankhah and Porté-Agel \(2014\)](#), as implemented within the PyWake software suite ([Pedersen et al., 2019](#)). Specifically, we use the predefined ‘IEA37SimpleBastankhahGaussian’ wind farm model available within PyWake. This model assumes a fixed wake expansion parameter of $k = 0.032$, and therefore neglects the influence of turbulence (or any other factors) on wake expansion ([Peña and Rathmann, 2014](#)). We further neglect the influence of air density on power production or

wakes. These assumptions enable us to isolate the influence of wind speed distributions on power and wakes, and we leave further exploration of their impact to future work.

The simulated power output of our ‘standard’ farm for speed s and rotation (or wind direction) d is denoted $P_{s,d}$. We then compute the mean power for each wind speed as

$$P_s = \frac{1}{n_{\text{dir}}} \sum_d P_{s,d}, \quad (5)$$

where n_{dir} is the number of wind directions, for which we choose 36, or bins of 10° . This mean power is then combined with the marginal wind speed distribution f_s , to produce the final ‘waked’ capacity factor, given by

$$\text{CF}_{\text{waked}} = 100\% \cdot \frac{1}{NP_{\text{max}}} \sum_s f_s P_s, \quad (6)$$

where $N = 100$ is the total number of wind turbines. We emphasise that by computing the capacity factor in this way, we are discarding all information about the wind direction distribution, and isolating the influence of the wind speed distribution. This allows for greater insight into the influence of wind speed distribution on power and wake effects, and reduces the sensitivity of the results to our choice of wind turbine layout within our ‘standard’ farm.

As well we the raw $\text{CF}_{\text{ambient}}$ and CF_{waked} values, we also present results for the capacity factor lost to wakes, given by

$$\text{CF lost} = \text{CF}_{\text{waked}} - \text{CF}_{\text{bg}}, \quad (7)$$

and the percentage of power lost to wakes, given by

$$\% \text{ losses} = 100\% \cdot (\text{CF}_{\text{waked}} - \text{CF}_{\text{bg}}) / \text{CF}_{\text{bg}}. \quad (8)$$

2.3. Mapping layout optimisation potential

The distribution of wind directions at a given location influences the optimal array layout. A highly focused wind direction distribution presents the possibility of mitigating wake losses by placing downstream turbines outside of the wake of upstream turbines. For uniformly distributed wind directions, however, we expect to find significantly less potential for optimisation.

We first investigate the variation in wind direction spread across EEZs, based on the ERA-5 reanalysis data. As a measure of wind direction spread, we use the circular standard deviation of the wind direction.

We then estimate the optimisation potential at each grid cell within the model domain. This is based on taking the ‘standard’ farm as a starting point, and optimising using the TopFarm Python package (Réthoré et al., 2014). This uses PyWake to estimate power for a given array layout, and interfaces with SciPy to perform a gradient-based optimisation of the position of each turbine, to maximise total power output. We define the optimisation potential as

$$\text{Opt potential} = 100\% \cdot \frac{\text{CF}_{\text{opt}} - \text{CF}_{\text{waked}}}{\text{CF}_{\text{waked}}}, \quad (9)$$

where CF_{waked} is given by equation (6) and CF_{opt} is obtained by optimisation using TopFarm. Note that for consistency with the other results we present, CF_{waked} is computed by averaging the wake effects over all rotations of the initial wind farm, which has a square grid layout. However, the optimal layout design is based on optimising from a single initial condition in which the farm grid layout is aligned with the mean wind direction.

Since there are approximately 300,000 grid cells within the global EEZs at the resolution we consider, the computational cost associated with optimising the array layout of the 100-turbine farm

for every grid cell is prohibitive. To mitigate this, we first coarsen the grid by a factor of 4 in each dimension, for a total of 18,491 grid cells. The coarsening discards data from unselected grid cells, since spatial averaging would produce artificially smooth wind roses. We also choose to perform the optimisation on a 25-turbine farm, with a 5 by 5 grid layout, rather than the full 100-turbine farm. This reduces the computational cost sufficiently to enable this global analysis. We further perform the optimisation on the full 100-turbine problem for a subset of 288 grid cells, obtained by coarsening the grid by a factor of 32 in each dimension. For each of the 25-turbine and 100-turbine problems, we obtain the optimisation potential given by equation (9). For the grid cells which appear in both datasets, we find a strong linear relationship between the optimisation potentials for the 25-turbine and 100-turbine problems, and therefore train a linear regression model to map from one to the other. Using this model, we then estimate the 100-turbine optimisation potential on the finer grid, on which we have run the 25-turbine optimisation. Further detail regarding the linear regression model is provided in [Appendix A](#).

2.4. Mapping future changes due to climate

The climate projection datasets used were described in section [2.1.2](#), including extrapolation to 100 m, and bias correction against ERA-5 data.

We restrict our analysis of climate change effects to the influence of wind speed distribution. For each climate model, we follow the method of section [2.2](#) to compute the ambient and ‘waked’ farm capacity factors, for both the ‘historical’ and future periods. From these, we firstly compute the projected change in ambient resource, as

$$100\% \cdot \frac{\widehat{CF}_{\text{ambient}} - CF_{\text{ambient}}}{CF_{\text{ambient}}}, \quad (10)$$

where $\widehat{CF}_{\text{ambient}}$ denotes the ambient CF for the future period. We secondly compute the projected change in wake-induced losses, as

$$\widehat{\% \text{ losses}} - \% \text{ losses}, \quad (11)$$

where the hat again indicates the future period.

The results we present within this study are based on the mean changes across the ensemble of 10 climate model projections. In order to identify robust changes, we isolate grid cells for which the sign of the projected changes is the same across at least 8 of the 10 models.

3. Results & discussion

3.1. Mapping wake effects

Figure [1\(a\)](#) shows the global distribution of ambient capacity factors, for the 10 MW reference turbine, based on ERA-5 data from our ‘historical’ period of 1995–2014. Consistent with well-established global wind climatology ([Zheng et al., 2018](#)), winds are strongest in the mid-latitudes, and in particular we find very high ambient capacity factors for latitudes between -40 and -60. Wind resources are smallest in the tropics. This result constitutes the most basic form of wind resource mapping, where we are interested only in the mean ambient wind power.

Figure [1\(b\)](#) shows the global distribution of the capacity factor lost to intra-farm wakes for the 10 by 10 reference array averaged over 36 orientations, given by equation [\(7\)](#). Figure [1\(c\)](#) shows the % losses given by equation [\(8\)](#). Comparing with figure [1\(a\)](#), in general we find that regions of high (low) ambient resource coincide with % losses of low (high) magnitude. Since wake losses are negative, this amounts to a positive correlation between ambient CF and % losses.

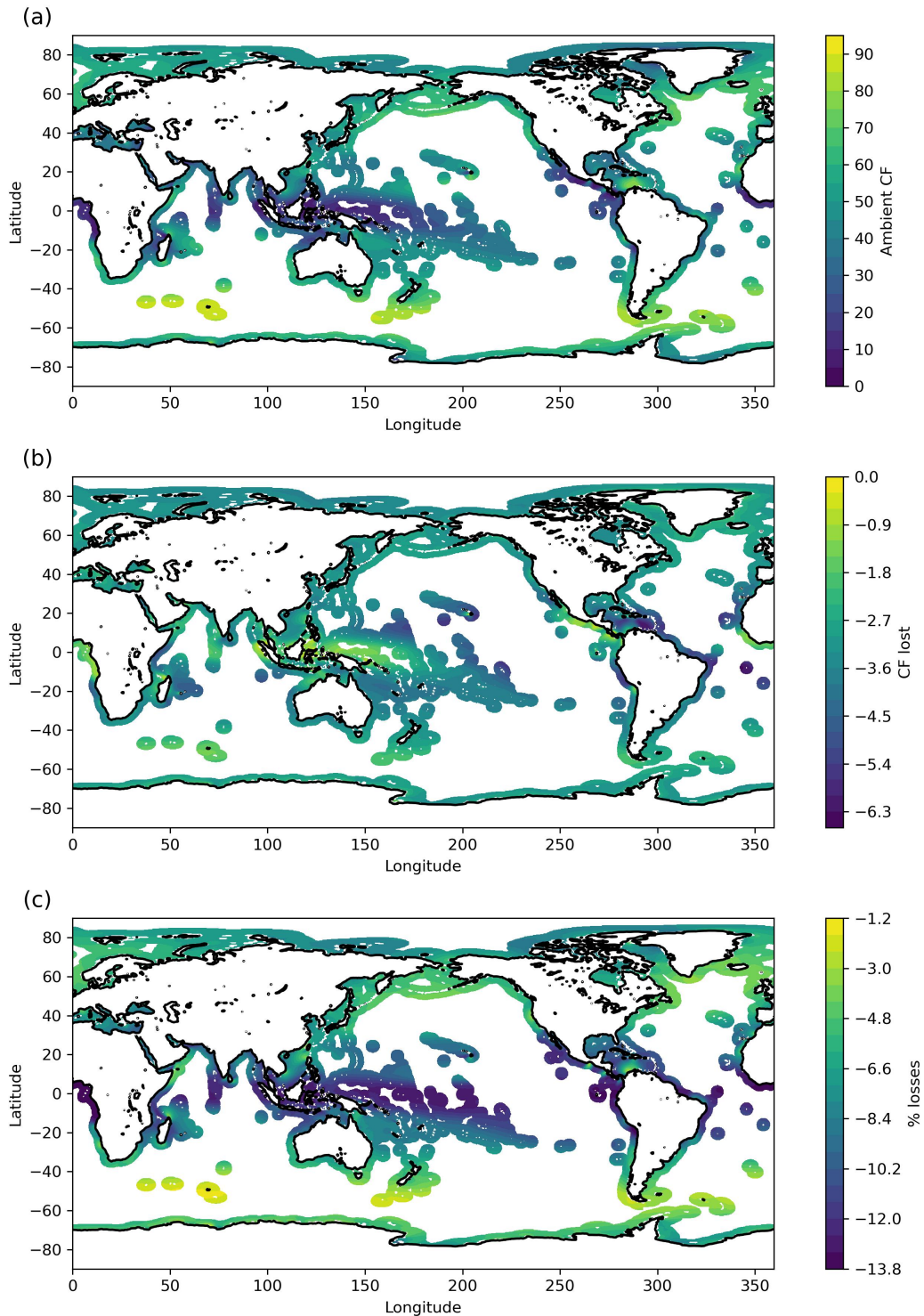


Figure 1: (a): Ambient capacity factor within all EEZs globally. (b): Capacity factor lost to intra-farm wakes, given by equation (7). (c): % losses, defined by equation (8).

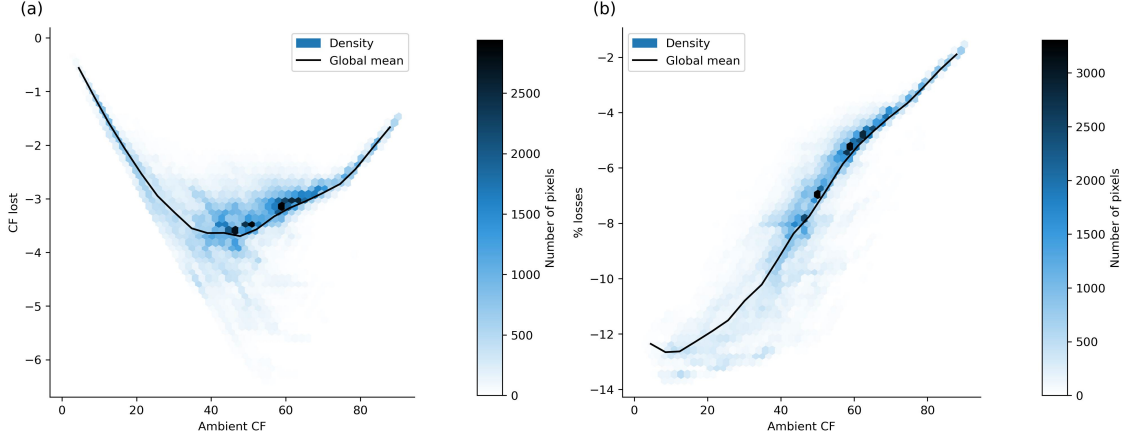


Figure 2: (a) CF lost, and (b) % power losses, due to intra-farm wakes, as a function of ambient CF. Solid lines show the global mean losses as a function of ambient CF. Broadly, there is a positive correlation between % losses and ambient CF. Note that losses are negative, hence a region with greater ambient CF typically experiences wake-induced losses of a smaller relative magnitude. This means that, in terms of absolute CF lost, for very large ambient CFs there is a drop-off in the magnitude of the losses. There is also a significant spread in losses for a given ambient CF, particularly for ambient CFs in the range 40–60%.

Investigating this relationship further, figure 2 shows the relationship between the ambient CF and (a) CF lost to wakes, and (b) % wake losses. The solid lines show the global mean losses, as a function of ambient CF. Focusing on figure 2(a), for low ambient CFs, we find a near-linear relationship, or equivalently in figure 2(b) the % losses initially change slowly with respect to ambient CF. However, for moderate ambient CFs of around 30% or higher, we find a bifurcation in figure 2(a). For most locations, the CF lost begins to reduce in magnitude (closer to zero) with increasing ambient CF. This can be explained by the decreasing fraction of wind speeds which fall between the cut-in and rated speeds of our reference wind turbine (3 and 11 m s^{-1} respectively), where wake effects are most significant. Most regions with higher average wind speeds produce greater ambient power, and also spend less time in this wake-sensitive interval, resulting in a reduction in absolute CF lost. However, there are some regions for which the near-linear relationship between ambient CF and CF lost continues, resulting in much greater wake losses. Looking at regions with ambient CF of, for example, 55–60%, there is a very broad spread of CF lost, and hence net CF which is extracted by our ‘standard’ farm.

Figure 3 reproduces the results of figure 2, but presents results aggregated per country, with selected countries highlighted. We observe that the United Kingdom, with access to high-resource offshore regions including in the North Sea and Irish Sea, has a high mean ambient CF of 65%, and relatively modest wake-induced losses of 4.5%. The United States, Australia and China have moderate ambient CF, and also moderate losses. We include Venezuela as a fairly extreme example of high wake losses which is fairly typical of Atlantic South America; it has a strong ambient resource of 56%, but suffers more than almost any other country in terms of absolute wake-induced losses, with 5.6% CF lost, equivalent to 10.3% losses. Brazil has the lowest ambient CF of the highlighted countries, and also suffers from greater than average losses, although is not as extreme as Venezuela.

Figure 4 presents the difference between the actual % losses, and the ‘global mean’ % losses as a function of ambient CF, shown by the solid line in figures 2(b) and 3(b). In general, the mid-latitudes suffer from smaller than average wake-induced losses (hence differences to the mean are positive), while the tropics suffer from larger losses (negative differences to the mean). We emphasise that these losses are relative to the global mean for the local ambient CF. We highlight particular regions

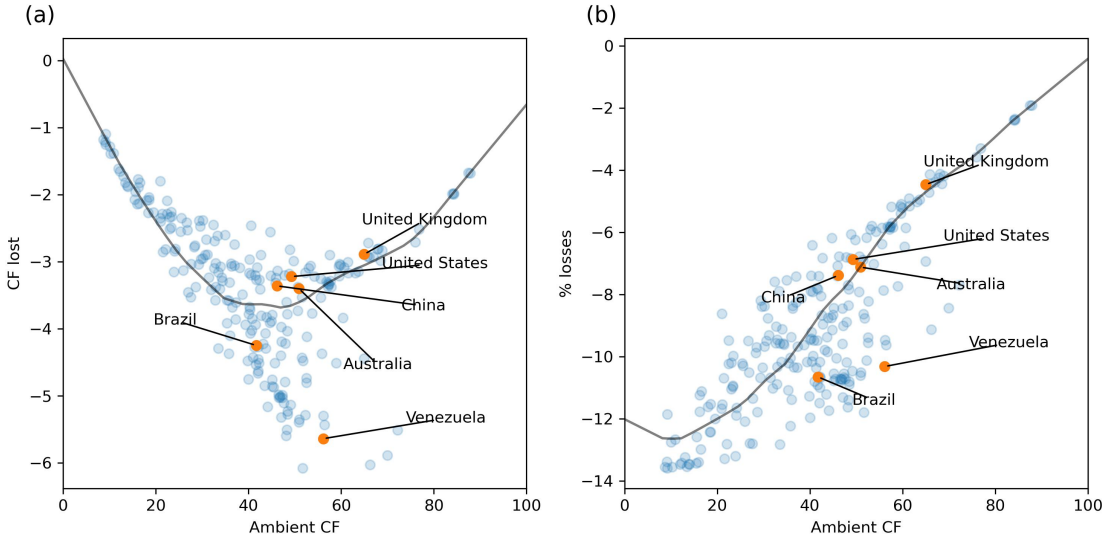


Figure 3: Average (a) CF lost, and (b) % power losses, versus ambient CF, aggregated per country. Lines show global mean.

of interest in figure 5. We find that Europe, including the Baltic and Mediterranean seas, possesses strong ambient resources, and favourable wake-induced losses. The US East Coast has moderate ambient resource and also has favourable losses. The US West Coast has stronger ambient resource than the East Coast. Near-shore regions exhibit favourable losses, but for regions further offshore the losses are stronger. Australia, with such a large spatial footprint, has a very broad range of ambient CFs, although some of the higher-resource regions coincide with larger-than-average wake-induced losses. India has fairly low ambient resource but mostly favourable wake losses. China has moderate ambient CFs, with slightly smaller-than-average wake effects. Atlantic South America suffers from some of the worst wake-induced losses. As identified in figure 3, Venezuela has strong ambient resource but very large wake-induced losses. Brazil similarly suffers from significant losses, as does most of the Atlantic coast of Colombia. These two regions were considered ‘markets to watch’ by [GWEC \(2023\)](#); these results suggest that a different approach to planning and design may be required, compared with Europe, due to the stronger wake effects experienced.

Overall, these results reveal the inadequacy of any (global) resource assessment which neglects wake effects, or which assumes spatially uniform losses. Neither absolute or percentage losses are spatially uniform. Both exhibit overall trends with respect to ambient CF, but there remains significant variation even among locations with the same ambient resource. In terms of absolute losses, there is a turning point where regions with greater ambient resource actually suffer from smaller absolute wake-induced losses; this pertains mostly to middle-latitude regions. In contrast, tropical regions with moderate to high ambient resource are likely to suffer from the largest wake-induced losses, with tropical South America particularly impacted.

3.1.1. Explaining the spatial variation in wake-induced losses

To explain the observed spatial variation in wake-induced losses, we must inspect specific wind speed distributions, in comparison to the turbine power and thrust curves. Figure 6 shows the mean wind speed distributions for Europe (including the Baltic and Mediterranean seas), and Venezuela, which was identified above as a country that experiences very high losses. The ambient capacity factors for these regions are very similar (55.8% for Europe, 56.1% for Venezuela), but the CF lost to wakes differs significantly (-2.9% for Europe, -5.6% for Venezuela). This is due to their

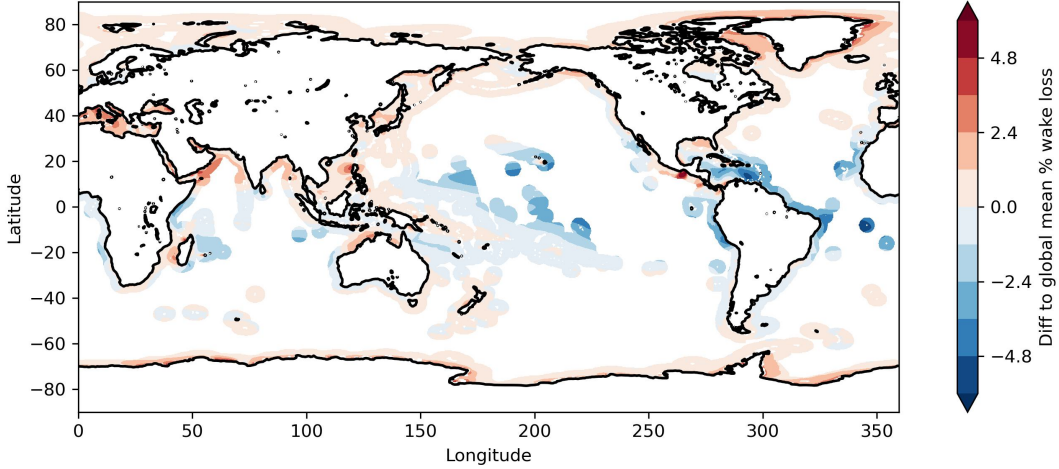


Figure 4: Difference between actual % loss and global mean % losses based on the fitted function in figure 2(b). Further detail for specific regions is shown in figure 5. Broadly, larger wake losses (negative values) are found nearer the equator.

differing wind speed distributions, as shown in figure 6. Venezuela exhibits a far narrower wind speed distribution than Europe, coinciding with the most wake-sensitive part of the turbine power and thrust curves (figure 7), which is between around 3 and 11 m s^{-1} . In Europe, a substantial part of the wind speed distribution sits above 11 m s^{-1} , where power output is at its maximum and is insensitive to wake effects.

This influence of the wind speed distribution on wake effects can be more formally explained by considering one-dimensional momentum theory (see e.g. [Kulunk \(2011\)](#)). The thrust coefficient of a turbine C_t can be related to the axial induction factor a , by

$$C_t = 4a(1 - a). \quad (12)$$

Given the wind turbine thrust curve data for our selected turbine model (see figure 7), we can thus derive a as a function of upstream wind speed. Neglecting wake expansion, the reduction in wind speed downstream of a wind turbine is then given by

$$U_w = U_\infty(1 - 2a), \quad (13)$$

where U_w is the wind speed in the wake, and U_∞ is the upstream wind speed. The reduction in wind speed is therefore given by

$$\Delta U = -2aU_\infty. \quad (14)$$

Given the turbine power curve $P(U)$, the reduction in power at a downstream turbine can then be estimated as

$$\Delta P(U_\infty) = \frac{dP}{dU} \Big|_{U_\infty} \Delta U = -2a \frac{dP}{dU} \Big|_{U_\infty} U_\infty. \quad (15)$$

Figure 8 shows this ΔP estimate as a function of wind speed. This is consistent with our earlier statements regarding the most important wind speed interval for wake effects, between around 3 and 11 m s^{-1} . Figure 8 also shows the actual average power lost per turbine by the ‘standard’ farm we study within this work, as a function of wind speed, as simulated using PyWake. Although $\Delta P(s)$ corresponds to the theoretical power lost by a single turbine downstream of another, neglecting wake expansion, it is clear that it is a good indicator of wake-induced losses at a given wind speed.

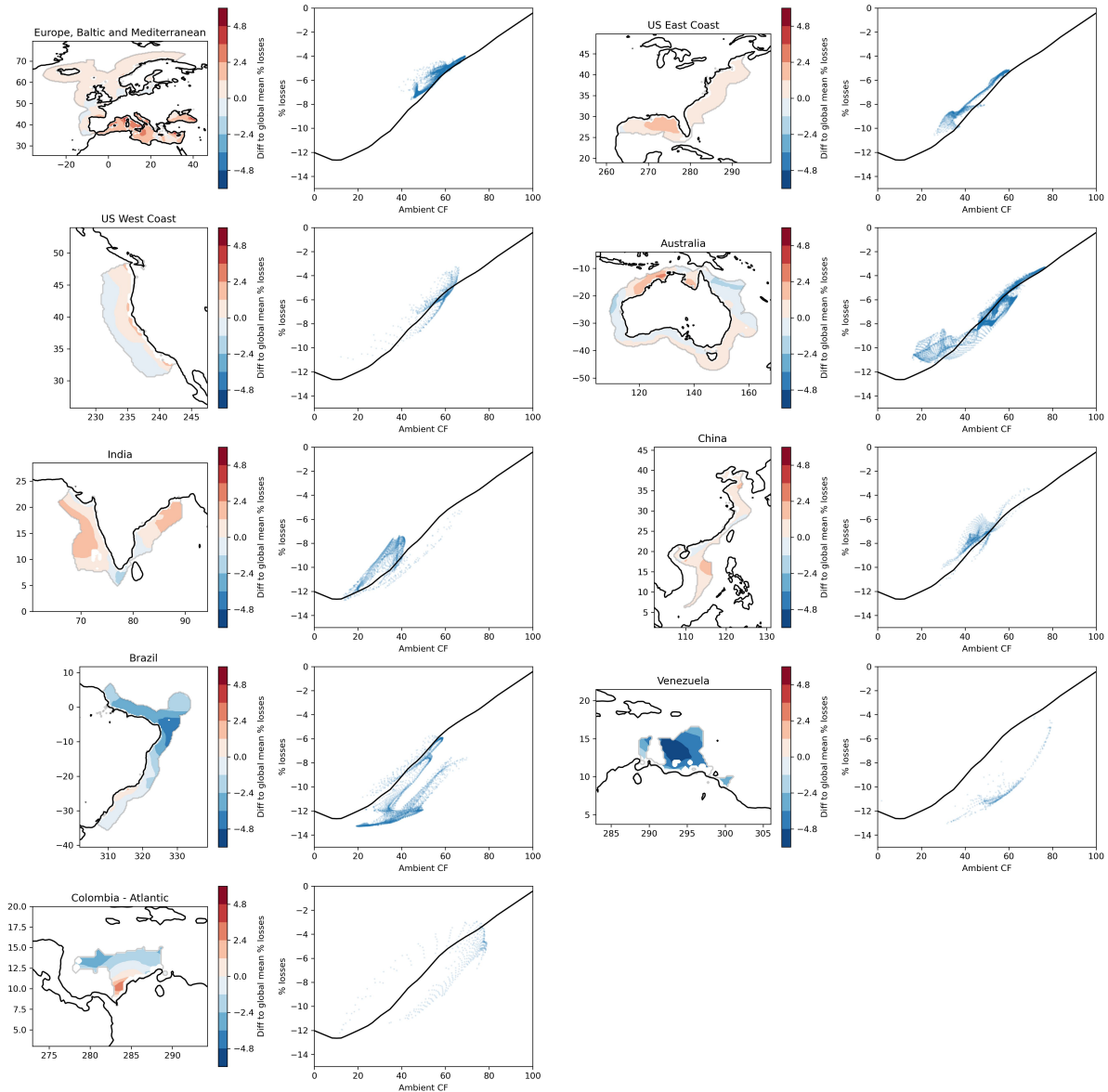


Figure 5: Ambient CF, % losses and differences to global mean % losses, for selected regions and countries.

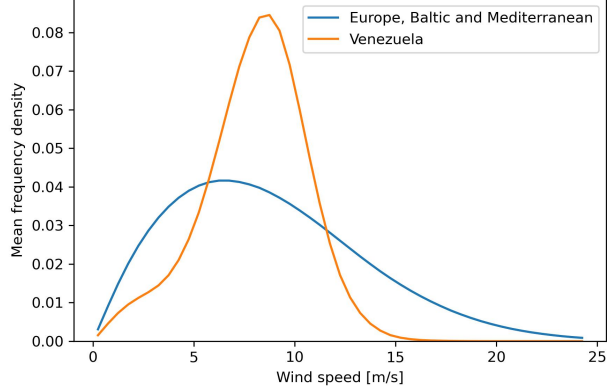


Figure 6: Mean wind speed distributions for Europe and Venezuela.

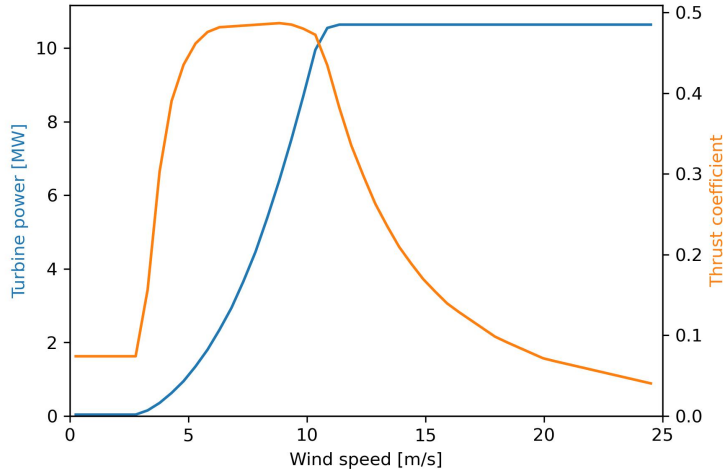


Figure 7: Power and thrust curves for the 10 MW reference turbine we use within this work ([Bortolotti et al., 2019](#)).

To derive a theoretical estimator for the overall mean wake-induced losses, we combine this $\Delta P(s)$ with the wind speed distribution at a given location f_s . Specifically, we calculate

$$\sum_s \Delta P(s) f_s. \quad (16)$$

We find that this quantity is very strongly correlated with the simulated wake losses, with an R^2 coefficient of 0.98.

We note that this formulation does not depend on the total capacity or layout of the wind farm, but only on the power and thrust curves of the selected turbine. It follows that turbine models with different thrust and power curves will produce a different spatial pattern of wake-induced losses. It may further be possible to mitigate losses by careful selection of turbine types appropriate to the wind speed distribution at the site where they will be deployed. Further exploration of the wake response for different turbine types is beyond the scope of the present study but will be considered in future work.

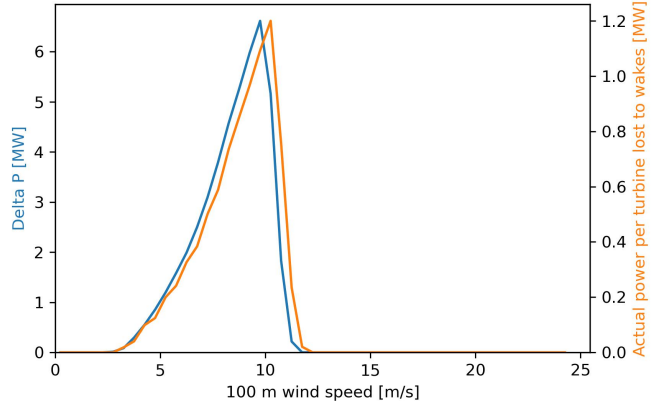


Figure 8: ΔP metric, given by equation (15). This approximates the theoretical power lost by a downstream turbine, for a given upstream wind speed. The secondary y axis shows the power loss by the ‘standard’ farm, as a function of wind speed, as simulated using PyWake. The region of wind speeds with greatest wake effects is between the cut-in and rated speeds, or around $3 - 11 \text{ m s}^{-1}$. The dotted lines indicate the wind speed distributions for Europe and Venezuela, from figure 6, highlighting the significant overlap between the wind speeds for Venezuela, and the ΔP metric.

3.2. Mapping layout optimisation potential

Figure 9 shows the global distribution of the circular standard deviation of the wind direction. The narrowest wind direction distributions are found near the equator, where the wind climate is dictated by the trade winds. Mid-latitudes experience a broader spread of wind directions.

Figure 10 shows the global distribution of the array layout optimisation potential, which is defined as the percentage improvement in mean power which can be obtained by an optimised layout, compared with the initial square farm layout. There is a negative correlation between wind direction standard deviation and optimisation potential. That is, narrower wind speed distributions are more conducive to array layout optimisation. We find the greatest optimisation potentials in northern South America, particularly on the western (Pacific) coast.

Comparing the optimisation potential of figure 10 with the global distribution of excess wake losses of figure 4, we find that the regions (mostly equatorial) where the wake losses are particularly high also have the greatest optimisation potential. This is also shown in figure 11, which should be compared with figure 2. Mean losses at all ambient CFs are improved by optimisation. Looking at the absolute losses (figs 2(a) and 11(a)), the optimisation has the greatest benefit for ambient CFs around 50–60%. In terms of percentage losses (figs 2(b) and 11(b)), the greatest improvements are found for ambient CFs of around 10–40%.

Overall, these results reveal that array layout optimisation has the potential to mitigate wake losses, and that the mitigation potential is often greatest in regions where wake losses are most severe. As explained in section 3.1.1, the higher wake losses in regions such as Venezuela are due to the narrower wind speed distribution. The results of this section show that these regions are also associated with narrower wind direction distributions, leading to greater mitigation opportunities via array layout optimisation.

These results implicitly assume that the wind distribution which is assumed during array design is applicable across the lifetime of the farm. Alternatively, climate projections could be used as the basis for robust array design with respect to future changes in wind distributions. However, this is beyond the scope of this study and is left for future work.

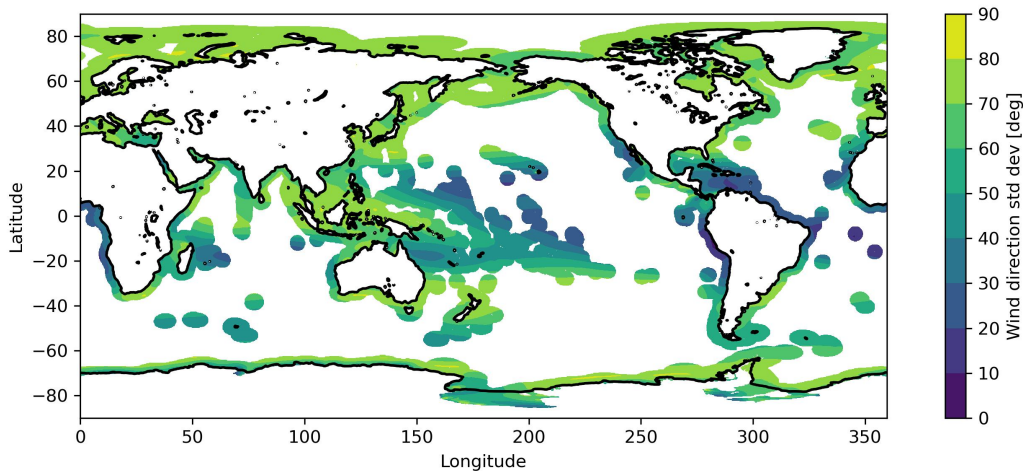


Figure 9: Circular standard deviation of wind direction. The wind direction distribution is narrowest nearer the equator.

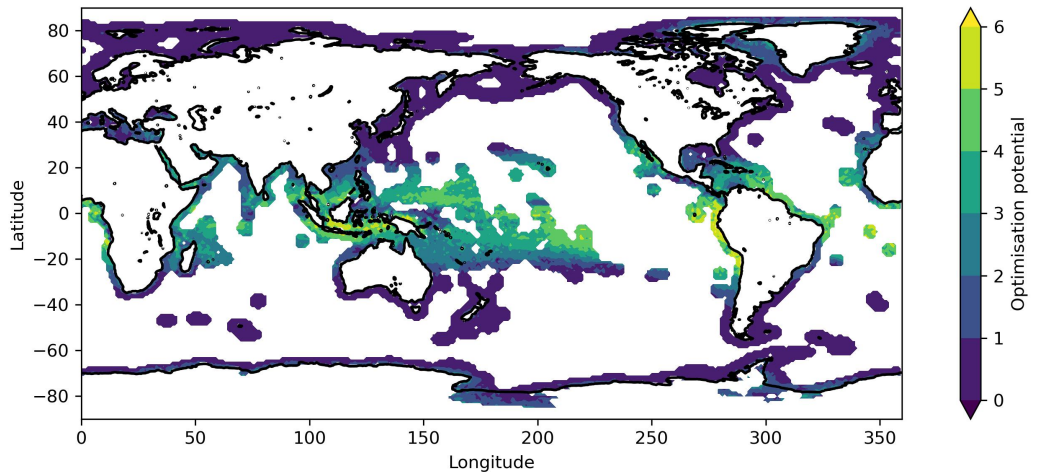


Figure 10: Optimisation potential. The greatest optimisation potentials are found in regions with the narrowest wind direction distributions, which tend to be found nearer the equator; see figure 9.

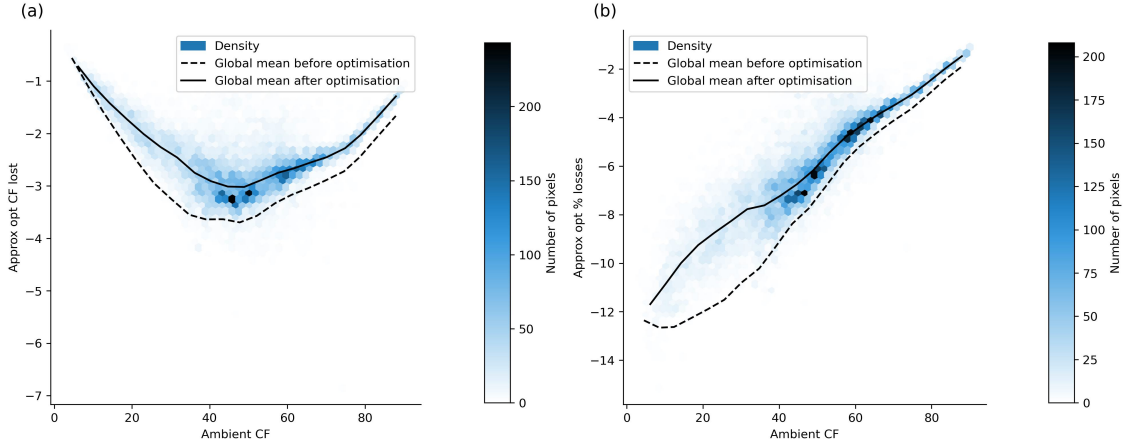


Figure 11: (a) CF lost, and (b) % power losses, due to intra-farm wakes, as a function of ambient capacity factor, after optimising wind farm layout. The dashed lines indicate the global means prior to optimisation, from figure 2.

3.3. Mapping future changes due to climate

Figure 12(a) shows the mean projected percentage change in ambient capacity factor across the 10 climate models, between the ‘historical’ climate, and 2081–2100 under the SSP585 scenario. Only grid cells with a statistically significant change are shown, where our significance criterion is that at least 8 out of the 10 climate models show the same sign of change. The result is broadly consistent with the global analysis of Ibarra-Berastegui et al. (2023), as well as with other regional studies. We observe statistically significant decreases in offshore wind resource across both Europe (consistent with (Carvalho et al., 2021)) and the US (consistent with Martinez and Iglesias (2022a)). We find a decrease in resource offshore of Northern China, which is consistent with Zhang and Li (2021); Deng et al. (2024), although we do not find statistically significant increases in south China. We find decreasing resources on the west coast of India (Basak et al., 2023), as well as most of Australia (Fournier et al., 2023). Our projections around South America are also consistent with the study of de Souza Ferreira et al. (2024).

Figures 13 and 14 show the relationship between the % projected change in ambient CF, and % losses, per grid cell (figure 13), and aggregated per country (figure 14). For the aggregation by country, the significance is determined on a per-country basis, rather than by aggregation over only the significant grid cells belonging to each country. Both indicate a positive correlation between change in ambient CF, and change in % wake losses. This is consistent with the trend found in section 3.1, and in particular figure 2(b).

The majority of grid cells/countries fall into the lower left quadrant of figures 13 and 14, indicating that ambient resource decreases, but that percentage wake-induced losses increase in magnitude, exacerbating the climate effect. Figure 15 indicates the spatial distribution of these grid cells. These regions include the northern Atlantic, impacting the US, Atlantic Canada, Greenland, Iceland, Ireland and the UK, as well as the US west coast, parts of Australia, India and China, southern Chile, and a number of island states in the southern Pacific. In these regions, decreases in ambient wind resource due to climate change are exacerbated by an increase in the magnitude of the percentage wake-induced losses.

In contrast, countries falling into the upper right quadrant of figures 13 and 14 are projected to both increase in ambient resource and improve in wake losses; these countries include Russia and Canada (driven mostly by strong increases in resource in the Arctic), as well as other isolated regions such as Pakistan and Oman. There are no countries which fall within either the upper left

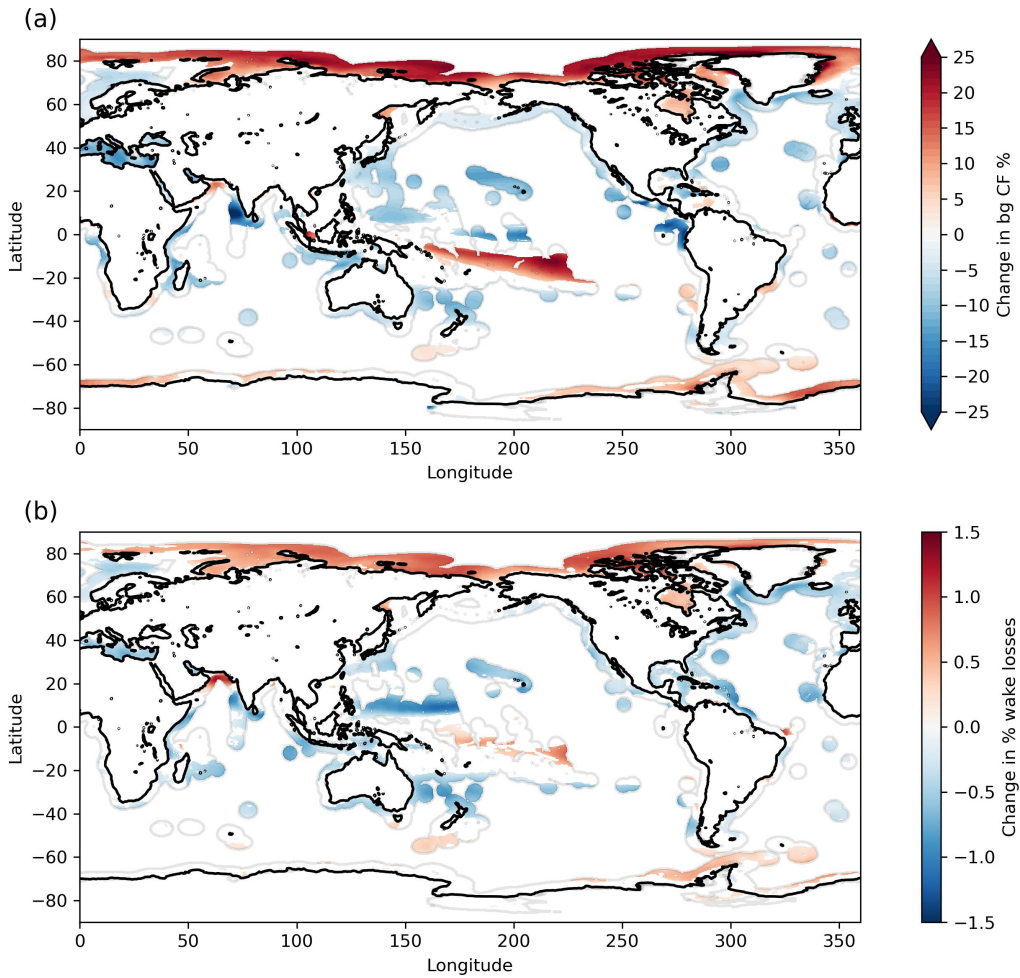


Figure 12: Mean projected changes over the 10 climate models in (a) ambient CF, (b) % wake-induced losses, from the historical to the future scenarios. Only grid cells with statistically significant changes are shown. The % change in power lost to wakes typically has the same sign as the % change in ambient CF.

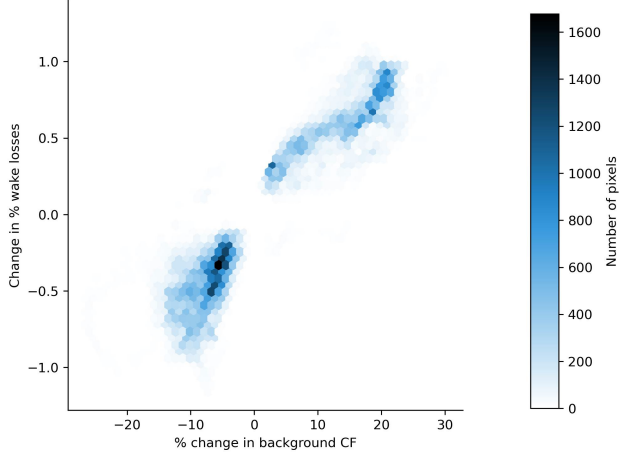


Figure 13: Change in % wake losses versus % change in ambient capacity factor, due to climate change. Only grid cells with significant changes are included.

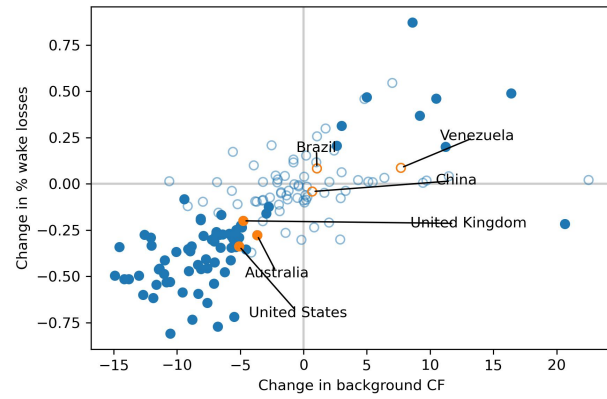


Figure 14: Change in % wake losses versus % change in ambient capacity factor, due to climate change, averaged by country. The mean is shown for all countries. Those with a statistically significant change are shown as solid points. Countries with insignificant changes are shown as hollow circles.

or lower right quadrants for which the statistical significance threshold is met, although there are a small number of individual grid cells meeting these criteria, as shown in figure 13.

Considering the globe as a whole, the direct climate impact on ambient power tends to have the greatest magnitude among the factors considered in this study, with magnitudes exceeding 25% for some regions, such as India. The magnitude of the baseline wake-induced losses (for the current climate) did not exceed 15%. Optimisation potentials reached up to 6–7%, while the indirect climate impact via wake effects has magnitudes of around 1%. However, we note that the relative size and significance of these effects varies by region. For example, there are some regions where optimisation potential exceeds the projected impact of climate change on ambient resource. This serves to further highlight that the challenges facing the offshore wind industry are highly region-dependent.

4. Conclusions

In this study, we have investigated global spatial variation in (i) ‘ambient’ offshore wind power potential, and (ii) intra-farm wake losses for a ‘standard’ offshore wind farm with a design represen-

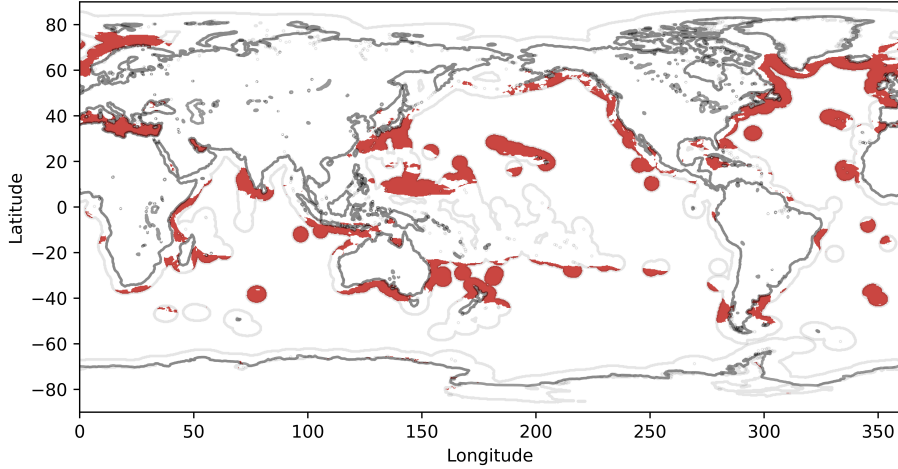


Figure 15: Map indicating regions where ambient wind resource is projected to decrease, and percentage wake-induced losses are projected to increase in magnitude.

tative of near-future installations. The spatial distribution of ambient wind power potential follows well-established global wind climatology, with resources greatest in the mid-latitudes, and lowest in the tropics. We find a strong correlation between ambient resources and percentage wake-induced losses; regions with greater ambient resource tend to lose a smaller fraction of their ambient power to wake effects. This trend exacerbates the spatial variation in ambient wind power density.

However, there remains a broad distribution of wake-induced losses even amongst locations with similar ambient resources. We find that the tropics are particularly badly impacted by wake effects, with the mid-latitudes relatively less impacted. That is, for a tropical and mid-latitude location with the same ambient wind resource, the mid-latitude location is likely to suffer from smaller wake-induced losses than the tropical location. We find that this can be explained by the specific wind speed distributions found in each region. The tropics tend to exhibit narrower wind speed distributions than mid-latitude regions, and thus a greater proportion of the wind speed distribution falls between the cut-in and rated speeds of the wind turbine, where power outputs are most sensitive to wake effects. We found that a simple analytic approach derived from one-dimensional momentum theory, based on combining the wind speed distribution with the turbine thrust and power curves, explains 98% of the variance in simulated wake-induced losses. It follows that wake effects will be sensitive to the choice of turbine model, and therefore that location-dependent selection of turbine models may help to mitigate wake-induced losses.

In assessing wind resources, either for early-stage wind farm planning or to derive inputs into power or energy system models, our results imply that it is not sufficient to assume spatially uniform wake-induced losses. The results also serve to highlight the natural advantages of northern Europe for offshore wind; this region has high ambient resources with relatively low wake-induced losses. In contrast, a number of emerging offshore wind markets are likely to be impacted by these enhanced (relative to mid-latitudes) wake-induced losses, including Brazil, Colombia, Australia and India.

This study also explored the impact of wind direction distribution on the spatial variation in wind power potential. A narrower spread of wind directions presents greater opportunity for the optimisation of array layout designs. The narrowest wind direction distributions tend to be found in the tropics where the wind climate is characterised by the trade winds. Although we found that the narrower wind speed distributions found in these regions leads to stronger wake effects, the narrower wind direction distribution presents greater opportunity for mitigation of these losses via

array layout optimisation. Although layout optimisation can only recover a fraction of the potential power lost to wakes, this result reveals the greater importance attached to layout optimisation in the tropics, compared with the mid-latitudes.

Finally, we assessed future changes in wind power potential and wake-induced losses, due to climate change. Based on the SSP585 scenario for the years 2081–2100, compared with a ‘historical’ period of 1995–2014, much of the globe shows a small but significant decrease in ambient wind resource. This includes Europe and China, the two regions with the greatest current offshore wind capacity. The main exceptions to this are the polar regions and in particular the Arctic, where resources are projected to increase. As for the current climate, we find a correlation between changes in ambient wind resource, and percentage power lost to wakes. This means that regions where wind resources decrease due to climate change are also likely to suffer from greater percentage wake losses, exacerbating the climate effect. Therefore, in assessing climate impacts on wind resources, it is not sufficient to assume that wake-induced losses will remain the same under a changing climate.

The results of this study have the potential to inform the transfer of knowledge from regions such as Europe, where offshore wind is relatively mature, to emerging markets such as in South America and Southeast Asia. The results highlight the different challenges likely to be experienced in efficiently harnessing wind resource in different regions, as well as the significance of layout optimisation, and potential future climate impacts.

There are a number of avenues for further work. Firstly, this study considered only a single wind farm configuration, and in particular a single turbine model. As discussed above, this has an impact on the simulated wake-induced losses, and warrants further investigation. Secondly, the layout optimisation in this work has considered only a fixed number of turbines, and optimised the total power generated by the farm. Alternatively, optimising the levelised cost of energy with respect to a variable number of turbines might lead to mitigation of wake impacts, for example by reducing the installed capacity density in regions more strongly affected by wakes. Finally, we have focused here on intra-farm wake effects. Recent literature has highlighted the significance of inter-farm wake effects, which would add a further spatial (and directional) component to maps of wake-induced losses, as well as additional uncertainty with respect to unknown future build-out, which would need to be considered alongside uncertain climate change.

Acknowledgements

We acknowledge HPC resources and support from the Imperial College Research Computing Service (<http://doi.org/10.14469/hpc/2232>).

References

- M. Abdullah, S. Ahmad, A. Kanwal, M. Farhan, U. B. Saeed, T. Ali, I. Amin, et al. An approach to assess offshore wind power potential using bathymetry and near-hub-height reanalysis data. *Ocean Engineering*, 280:114458, 2023.
- M. Akperov, A. V. Eliseev, A. Rinke, I. I. Mokhov, V. A. Semenov, M. Dembitskaya, H. Matthes, M. Adakudlu, F. Boberg, J. H. Christensen, et al. Future projections of wind energy potentials in the arctic for the 21st century under the rcp8. 5 scenario from regional climate models (arctic-cordex). *Anthropocene*, 44:100402, 2023.
- C. L. Archer, A. Vasel-Be-Hagh, C. Yan, S. Wu, Y. Pan, J. F. Brodie, and A. E. Maguire. Review and evaluation of wake loss models for wind energy applications. *Applied Energy*, 226:1187–1207, 2018.

S. Ashwin Renganathan, R. Maulik, S. Letizia, and G. V. Iungo. Data-driven wind turbine wake modeling via probabilistic machine learning. *Neural Computing and Applications*, pages 1–16, 2022.

G. Bandoc, R. Prăvălie, C. Patriche, and M. Degeratu. Spatial assessment of wind power potential at global scale. a geographical approach. *Journal of Cleaner Production*, 200:1065–1086, 2018.

D. Basak, G. Nagababu, H. Puppala, J. Patel, and S. V. A. Kumar. Foreseeing the spatio-temporal offshore wind energy potential of India using a differential weighted ensemble created using CMIP6 datasets. *Regional Studies in Marine Science*, 65:103066, 2023.

M. Bastankhah and F. Porté-Agel. A new analytical model for wind-turbine wakes. *Renewable energy*, 70:116–123, 2014.

E. F. Benmoufok, S. C. Warder, E. Zhu, B. Bhaskaran, I. Staffell, and M. Piggott. Improving wind power modelling through granular spatial and temporal bias correction of reanalysis data. *Available at SSRN 4856203*, 2024.

P. Bortolotti, H. C. Tarres, K. Dykes, K. Merz, L. Sethuraman, D. Verelst, and F. Zahle. Iea wind tcp task 37: Systems engineering in wind energy-wp2. 1 reference wind turbines. 2019.

J. Bosch, I. Staffell, and A. D. Hawkes. Temporally explicit and spatially resolved global offshore wind energy potentials. *Energy*, 163:766–781, 2018.

J. Bosch, I. Staffell, and A. D. Hawkes. Global levelised cost of electricity from offshore wind. *Energy*, 189:116357, 2019.

B. Cañadillas, M. Beckenbauer, J. J. Trujillo, M. Dörenkämper, R. Foreman, T. Neumann, and A. Lampert. Offshore wind farm cluster wakes as observed by long-range-scanning wind lidar measurements and mesoscale modeling. *Wind Energy Science*, 7(3):1241–1262, 2022.

D. Carvalho, A. Rocha, X. Costoya, M. DeCastro, and M. Gómez-Gesteira. Wind energy resource over europe under CMIP6 future climate projections: What changes from CMIP5 to CMIP6. *Renewable and Sustainable Energy Reviews*, 151:111594, 2021.

A. Cherchi, P. G. Fogli, T. Lovato, D. Peano, D. Iovino, S. Gualdi, S. Masina, E. Scoccimarro, S. Materia, A. Bellucci, et al. Global mean climate and main patterns of variability in the cmcc-cm2 coupled model. *Journal of Advances in Modeling Earth Systems*, 11(1):185–209, 2019.

X. Costoya, M. DeCastro, D. Carvalho, and M. Gómez-Gesteira. On the suitability of offshore wind energy resource in the united states of america for the 21st century. *Applied Energy*, 262:114537, 2020.

G. Danabasoglu, J.-F. Lamarque, J. Bacmeister, D. Bailey, A. DuVivier, J. Edwards, L. Emmons, J. Fasullo, R. Garcia, A. Gettelman, et al. The community earth system model version 2 (cesm2). *Journal of Advances in Modeling Earth Systems*, 12(2):e2019MS001916, 2020.

N. N. Davis, J. Badger, A. N. Hahmann, B. O. Hansen, N. G. Mortensen, M. Kelly, X. G. Larsén, B. T. Olsen, R. Floors, G. Lizcano, et al. The global wind atlas: A high-resolution dataset of climatologies and associated web-based application. *Bulletin of the American Meteorological Society*, 104(8):E1507–E1525, 2023.

G. W. de Souza Ferreira, M. Reboita, J. Ribeiro, V. Carvalho, M. Santiago, P. Silva, T. Baldoni, and C. de Souza. Assessment of the wind power density over South America simulated by CMIP6 models in the present and future climate. *Climate Dynamics*, 62(3):1729–1763, 2024.

M. deCastro, X. Costoya, S. Salvador, D. Carvalho, M. Gómez-Gesteira, F. J. Sanz-Larruga, and L. Gimeno. An overview of offshore wind energy resources in europe under present and future climate. *Annals of the New York Academy of Sciences*, 1436(1):70–97, 2019.

K. Deng, S. Yang, W. Liu, H. Li, D. Chen, T. Lian, G. Zhang, J. Zha, and C. Shen. The offshore wind speed changes in china: an insight into CMIP6 model simulation and future projections. *Climate Dynamics*, 62(5):3305–3319, 2024.

A. Devis, N. P. Van Lipzig, and M. Demuzere. Should future wind speed changes be taken into account in wind farm development? *Environmental Research Letters*, 13(6):064012, 2018.

Q. V. Dinh, Q.-V. Doan, T. Ngo-Duc, N. D. Duc, et al. Offshore wind resource in the context of global climate change over a tropical area. *Applied Energy*, 308:118369, 2022.

M. Dörenkämper, B. T. Olsen, B. Witha, A. N. Hahmann, N. N. Davis, J. Barcons, Y. Ezber, E. García-Bustamante, J. F. González-Rouco, J. Navarro, et al. The making of the new european wind atlas—part 2: Production and evaluation. *Geoscientific Model Development Discussions*, 2020:1–37, 2020.

J. P. Dunne, L. Horowitz, A. Adcroft, P. Ginoux, I. Held, J. John, J. P. Krasting, S. Malyshev, V. Naik, F. Paulot, et al. The gfdl earth system model version 4.1 (gfdl-esm 4.1): Overall coupled model description and simulation characteristics. *Journal of Advances in Modeling Earth Systems*, 12(11):e2019MS002015, 2020.

C. N. Elkinton, J. F. Manwell, and J. G. McGowan. Algorithms for offshore wind farm layout optimization. *Wind engineering*, 32(1):67–84, 2008.

A. Energiewende, A. Verkehrswende, et al. Making the most of offshore wind: Re-evaluating the potential of offshore wind in the german north sea. *Agora Energiewende*, pages 1–81, 2020.

J. C. Fernández-Alvarez, X. Costoya, A. Pérez-Alarcón, S. Rahimi, R. Nieto, and L. Gimeno. Dynamic downscaling of wind speed over the north atlantic ocean using CMIP6 projections: implications for offshore wind power density. *Energy Reports*, 9:873–885, 2023.

A. Fernández-Guillamón, K. Das, N. A. Cutululis, and Á. Molina-García. Offshore wind power integration into future power systems: Overview and trends. *Journal of Marine Science and Engineering*, 7(11):399, 2019.

Flanders Marine Institute. The intersect of the Exclusive Economic Zones and IHO sea areas, version 4. 2020. doi: <https://doi.org/10.14284/402>. Available online at <https://www.marineregions.org/>.

A. Fournier, A. Martinez, and G. Iglesias. Impacts of climate change on wind energy potential in Australasia and South-East Asia following the Shared Socioeconomic Pathways. *Science of The Total Environment*, 882:163347, 2023.

J. Gea-Bermúdez, L. Kitzing, M. Koivisto, K. Das, J. P. Murcia León, and P. Sørensen. The value of sector coupling for the development of offshore power grids. *Energies*, 15(3):747, 2022.

P. Glaum, F. Neumann, and T. Brown. Offshore power and hydrogen networks for europe's north sea. *Applied Energy*, 369:123530, 2024.

T. Göçmen, P. Van der Laan, P.-E. Réthoré, A. P. Diaz, G. C. Larsen, and S. Ott. Wind turbine wake models developed at the technical university of denmark: A review. *Renewable and Sustainable Energy Reviews*, 60:752–769, 2016.

K. Gruber, P. Regner, S. Wehrle, M. Zeyringer, and J. Schmidt. Towards global validation of wind power simulations: A multi-country assessment of wind power simulation from merra-2 and era-5 reanalyses bias-corrected with the global wind atlas. *Energy*, 238:121520, 2022.

GWEC. Global Wind Energy Council Global Offshore Wind Report 2023. 2023.

GWEC. Global Wind Energy Council Global Offshore Wind Report 2024. 2024.

A. N. Hahmann, T. Sile, B. Witha, N. N. Davis, M. Dörenkämper, Y. Ezber, E. García-Bustamante, J. F. González-Rouco, J. Navarro, B. T. Olsen, et al. The making of the New European Wind Atlas—part 1: model sensitivity. *Geoscientific model development*, 13(10):5053–5078, 2020.

A. N. Hahmann, O. García-Santiago, and A. Peña. Current and future wind energy resources in the north sea according to CMIP6. *Wind Energy Science Discussions*, 2022:1–32, 2022.

C. B. Hasager, A. N. Hahmann, T. Ahsbahs, I. Karagali, T. Sile, M. Badger, and J. Mann. Europe's offshore winds assessed with synthetic aperture radar, ascat and wrf. *Wind Energy Science*, 5(1):375–390, 2020.

Q. Hassan, S. Algburi, A. Z. Sameen, J. Tariq, A. K. Al-Jiboory, H. M. Salman, B. M. Ali, M. Jaszczur, et al. A comprehensive review of international renewable energy growth. *Energy and Built Environment*, 2024.

I. Held, H. Guo, A. Adcroft, J. Dunne, L. Horowitz, J. Krasting, E. Shevliakova, M. Winton, M. Zhao, M. Bushuk, et al. Structure and performance of gfdl's cm4. 0 climate model. *Journal of Advances in Modeling Earth Systems*, 11(11):3691–3727, 2019.

H. Hersbach, B. Bell, P. Berrisford, S. Hirahara, A. Horányi, J. Muñoz-Sabater, J. Nicolas, C. Peubey, R. Radu, D. Schepers, et al. The era5 global reanalysis. *Quarterly Journal of the Royal Meteorological Society*, 146(730):1999–2049, 2020.

G. Ibarra-Berastegui, J. Sáenz, A. Ulazia, A. Sáenz-Aguirre, and G. Esnaola. CMIP6 projections for global offshore wind and wave energy production (2015–2100). *Scientific Reports*, 13(1):18046, 2023.

N. O. Jensen. *A note on wind generator interaction*. Risø National Laboratory, 1983.

H. Kawai, S. Yukimoto, T. Koshiro, N. Oshima, T. Tanaka, H. Yoshimura, and R. Nagasawa. Significant improvement of cloud representation in the global climate model mri-esm2. *Geoscientific Model Development*, 12(7):2875–2897, 2019.

A. C. Kheirabadi and R. Nagamune. A quantitative review of wind farm control with the objective of wind farm power maximization. *Journal of Wind Engineering and Industrial Aerodynamics*, 192:45–73, 2019.

E. Kulunk. Aerodynamics of wind turbines. In *Fundamental and advanced topics in wind power*. IntechOpen, 2011.

W.-L. Lee and H.-C. Liang. AS-RCEC TaiESM1. 0 model output prepared for CMIP6 ScenarioMIP. 2020.

D. Li, J. Feng, A. Dosio, J. Qi, Z. Xu, and B. Yin. Historical evaluation and future projections of 100-m wind energy potentials over cordex-east asia. *Journal of Geophysical Research: Atmospheres*, 125(15):e2020JD032874, 2020.

L. Li, J. Lin, N. Wu, S. Xie, C. Meng, Y. Zheng, X. Wang, and Y. Zhao. Review and outlook on the international renewable energy development. *Energy and Built Environment*, 3(2):139–157, 2022.

S. Li, M. Zhang, and M. D. Piggott. End-to-end wind turbine wake modelling with deep graph representation learning. *Applied Energy*, 339:120928, 2023.

T. Lovato, D. Peano, M. Butenschön, S. Materia, D. Iovino, E. Scoccimarro, P. Fogli, A. Cherchi, A. Bellucci, S. Gualdi, et al. CMIP6 simulations with the cmcc earth system model (cmcc-esm2). *Journal of Advances in Modeling Earth Systems*, 14(3):e2021MS002814, 2022.

J. K. Lundquist, K. K. DuVivier, D. Kaffine, and J. M. Tomaszewski. Costs and consequences of wind turbine wake effects arising from uncoordinated wind energy development. *Nature Energy*, 4(1):26–34, 2019.

A. Lyden, W. Sun, I. Struthers, L. Franken, S. Hudson, Y. Wang, and D. Friedrich. Pypsa-gb: An open-source model of great britain’s power system for simulating future energy scenarios. *Energy Strategy Reviews*, 53:101375, 2024.

A. Martinez and G. Iglesias. Wind resource evolution in europe under different scenarios of climate change characterised by the novel shared socioeconomic pathways. *Energy Conversion and Management*, 234:113961, 2021.

A. Martinez and G. Iglesias. Climate change impacts on wind energy resources in North America based on the CMIP6 projections. *Science of The Total Environment*, 806:150580, 2022a.

A. Martinez and G. Iglesias. Mapping of the levelised cost of energy for floating offshore wind in the european atlantic. *Renewable and Sustainable Energy Reviews*, 154:111889, 2022b.

A. Martinez, L. Murphy, and G. Iglesias. Evolution of offshore wind resources in northern europe under climate change. *Energy*, 269:126655, 2023.

E. J. N. Menezes, A. M. Araújo, and N. S. B. Da Silva. A review on wind turbine control and its associated methods. *Journal of cleaner production*, 174:945–953, 2018.

M. O. Molina, J. A. M. Careto, C. Gutiérrez, E. Sánchez, and P. M. M. Soares. The added value of high-resolution euro-cordex simulations to describe daily wind speed over europe. *International Journal of Climatology*, 43(2):1062–1078, 2022.

N. G. Mortensen, L. Landberg, O. Rathmann, H. Frank, I. Troen, and E. Petersen. Wind atlas analysis and application program (wasp). In *Wind Energy Department: Scientific and technical progress 1999-2000*. 2001.

W. A. Müller, J. H. Jungclaus, T. Mauritsen, J. Baehr, M. Bittner, R. Budich, F. Bunzel, M. Esch, R. Ghosh, H. Haak, et al. A higher-resolution version of the max planck institute earth system model (mpi-esm1. 2-hr). *Journal of Advances in Modeling Earth Systems*, 10(7):1383–1413, 2018.

R. P. Patel, G. Nagababu, S. S. Kachhwaha, and V. A. K. Surisetty. A revised offshore wind resource assessment and site selection along the indian coast using era5 near-hub-height wind products. *Ocean Engineering*, 254:111341, 2022.

M. M. Pedersen, P. van der Laan, M. Friis-Møller, J. Rinker, and P.-E. Réthoré. Dtuwindenergy/pywake: Pywake, Feb. 2019. URL <https://doi.org/10.5281/zenodo.2562662>.

A. Peña and O. Rathmann. Atmospheric stability-dependent infinite wind-farm models and the wake-decay coefficient. *Wind Energy*, 17(8):1269–1285, 2014.

M. D. Piggott, S. C. Kramer, S. W. Funke, D. M. Culley, and A. Angeloudis. Optimization of marine renewable energy systems. In *Comprehensive Renewable Energy, 2nd Edition*, volume 8, pages 176–220. Elsevier, 2022. ISBN 978-0-12-409548-9. doi: <https://doi.org/10.1016/B978-0-12-819727-1.00179-5>.

F. M. Pimenta, A. R. Silva, A. T. Assireu, V. d. S. e. Almeida, and O. R. Saavedra. Brazil offshore wind resources and atmospheric surface layer stability. *Energies*, 12(21):4195, 2019.

J. G. Powers, J. B. Klemp, W. C. Skamarock, C. A. Davis, J. Dudhia, D. O. Gill, J. L. Coen, D. J. Gochis, R. Ahmadov, S. E. Peckham, et al. The weather research and forecasting model: Overview, system efforts, and future directions. *Bulletin of the American Meteorological Society*, 98(8):1717–1737, 2017.

S. Purohit, E. Y. K. Ng, and I. F. S. A. Kabir. Evaluation of three potential machine learning algorithms for predicting the velocity and turbulence intensity of a wind turbine wake. *Renewable Energy*, 184:405–420, 2022.

P.-E. Réthoré, P. Fuglsang, G. C. Larsen, T. Buhl, T. J. Larsen, and H. A. Madsen. TOPFARM: Multi-fidelity optimization of wind farms. *Wind Energy*, 17(12):1797–1816, 2014.

M. Reyers, J. Moemken, and J. G. Pinto. Future changes of wind energy potentials over europe in a large CMIP5 multi-model ensemble. *International Journal of Climatology*, 36(2), 2016.

M. Samorani. *The wind farm layout optimization problem*. Springer, 2013.

B. Sanderse, S. Van der Pijl, and B. Koren. Review of computational fluid dynamics for wind turbine wake aerodynamics. *Wind energy*, 14(7):799–819, 2011.

J. Schneemann, A. Rott, M. Dörenkämper, G. Steinfeld, and M. Kühn. Cluster wakes impact on a far-distant offshore wind farm’s power. *Wind Energy Science*, 5(1):29–49, 2020.

M. Shadman, M. Roldan-Carvajal, F. G. Pierart, P. A. Haim, R. Alonso, C. Silva, A. F. Osorio, N. Almonacid, G. Carreras, M. Maali Amiri, et al. A review of offshore renewable energy in south america: current status and future perspectives. *Sustainability*, 15(2):1740, 2023.

R. Shakoor, M. Y. Hassan, A. Raheem, and Y.-K. Wu. Wake effect modeling: A review of wind farm layout optimization using jensen’s model. *Renewable and Sustainable Energy Reviews*, 58: 1048–1059, 2016.

P. M. Soares, D. C. Lima, and M. Nogueira. Global offshore wind energy resources using the new era-5 reanalysis. *Environmental Research Letters*, 15(10):1040a2, 2020.

I. Staffell and S. Pfenninger. Using bias-corrected reanalysis to simulate current and future wind power output. *Energy*, 114:1224–1239, 2016.

Z. Ti, X. W. Deng, and H. Yang. Wake modeling of wind turbines using machine learning. *Applied Energy*, 257:114025, 2020.

A. Vinhoza and R. Schaeffer. Brazil's offshore wind energy potential assessment based on a spatial multi-criteria decision analysis. *Renewable and Sustainable Energy Reviews*, 146:111185, 2021.

P. J. Volker, A. N. Hahmann, J. Badger, and H. E. Jørgensen. Prospects for generating electricity by large onshore and offshore wind farms. *Environmental Research Letters*, 12(3):034022, 2017.

E. Volodin, E. Mortikov, S. Kostrykin, V. Y. Galin, V. Lykossov, A. Gritsun, N. Diansky, A. Gusev, and N. Iakovlev. Simulation of the present-day climate with the climate model INMCM5. *Climate dynamics*, 49:3715–3734, 2017.

E. Volodin, E. Mortikov, A. Gritsun, V. Lykossov, V. Galin, N. Diansky, A. Gusev, S. Kostrykin, N. Iakovlev, A. Shestakova, et al. INM INM-CM4-8 model output prepared for CMIP6 ScenarioMIP. 2019.

S. C. Warder and M. D. Piggott. The future of offshore wind power production: wake and climate impacts. *under review at Applied Energy*, 2024.

C. V. Weiss, R. Guanche, B. Ondiviela, O. F. Castellanos, and J. Juanes. Marine renewable energy potential: A global perspective for offshore wind and wave exploitation. *Energy conversion and management*, 177:43–54, 2018.

J. Zhang and X. Zhao. A novel dynamic wind farm wake model based on deep learning. *Applied Energy*, 277:115552, 2020.

S. Zhang and X. Li. Future projections of offshore wind energy resources in china using CMIP6 simulations and a deep learning-based downscaling method. *Energy*, 217:119321, 2021.

C.-w. Zheng, Z.-n. Xiao, Y.-h. Peng, C.-y. Li, and Z.-b. Du. Rezoning global offshore wind energy resources. *Renewable energy*, 129:1–11, 2018.

C.-w. Zheng, X.-y. Li, X. Luo, X. Chen, Y.-h. Qian, Z.-h. Zhang, Z.-s. Gao, Z.-b. Du, Y.-b. Gao, and Y.-g. Chen. Projection of future global offshore wind energy resources using cmip data. *Atmosphere-ocean*, 57(2):134–148, 2019.

Appendix A. Linear regression model for optimisation potential

As described in section 2.3, to estimate the optimisation potential for our 100-turbine farm, we instead calculate the optimisation potential for a smaller 25-turbine farm, and train a model to predict the optimisation potential of a 100-turbine farm subject to the same wind rose.

The model is trained on a set of 288 wind roses. For each, we perform layout optimisation using TopFarm, for both the 25-turbine and 100-turbine wind farm cases. Figure A1 compares the optimisation potentials for each of these cases, showing a relationship which is close to linear. The 100-turbine farm tends to show slightly greater optimisation potential than the smaller 25-turbine farm. This is consistent with the larger farm experiencing stronger wake effects overall, and therefore having slightly greater scope for mitigation of wake-induced losses via optimisation.

To test the performance of a linear regression model to predict 100-turbine optimisation potential from 25-turbine optimisation potential, we divide the 288 optimisation cases into equal training and test datasets. The training dataset is used to train the model. Figure A2 compares the predicted

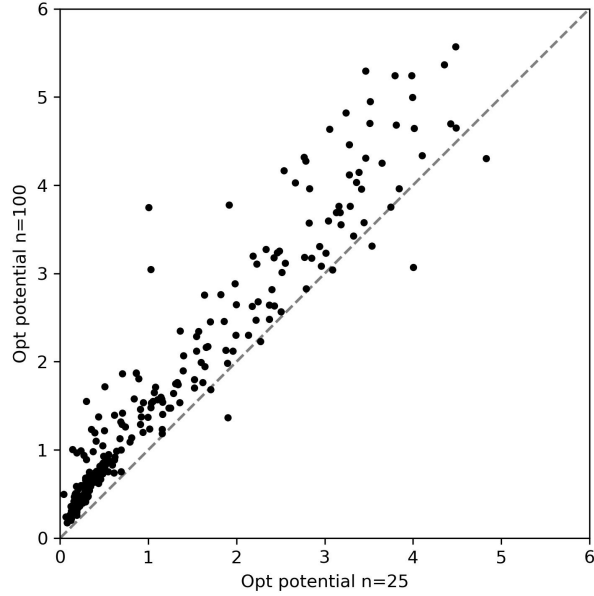


Figure A1: Comparison between optimisation potentials for 100-turbine ($n = 100$) and 25-turbine ($n = 25$) cases. There is a clear linear relationship.

and actual 100-turbine optimisation potentials for the test data. The root mean squared error is 0.4 percentage points. The accuracy of this model is sufficient to assess the overall global trends in optimisation potential.

Finally, the model is retrained using all 288 wind rose cases. The 25-turbine optimisation is performed for 18,491 grid cells with global coverage as described in section 2.3. The trained linear regression model is then used to predict the 100-turbine optimisation potential for all 18,491 grid cells.

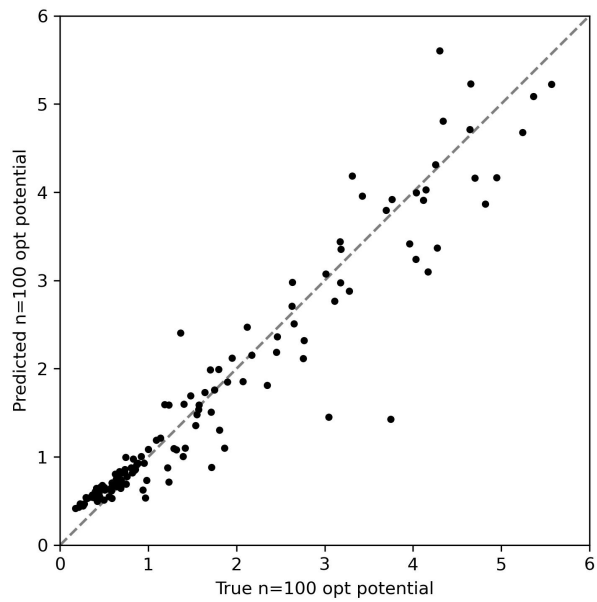


Figure A2: Predicted optimisation potential compared with actual optimisation potential, for the 100-turbine case. The root mean squared error is 0.4.